Materials and Energy Research Center
MERC

Contents lists available at ACERP

Advanced Ceramics Progress

Journal Homepage: www.acerp.ir

Original Research Article

Tailoring Bioactivity and Corrosion Properties of Plasma Electrolytic Oxidized Titanium Using GO-Silane Particles

Behnaz Hamrahi [a], Benyamin Yarmand [b, *], Abouzar Massoudi [c]

[a] *PhD, Department of Nanotechnology and Advanced Materials, Materials and Energy Research Center, Karaj, Iran*
[b] *Associate Professor, Department of Nanotechnology and Advanced Materials, Materials and Energy Research Center, Karaj, Iran*
[c] *Assistant Professor, Department of Semiconductors, Materials and Energy Research Center, Karaj, Iran*

* Corresponding Author Email: byarmand@merc.ac.ir (B. Yarmand)

URL: https://www.acerp.ir/article_161858.html

ARTICLE INFO

Article History:

Received 8 October 2022
Received in revised form 15 November 2022
Accepted 29 November 2022

Keywords:

GO-Silane
Plasma Electrolytic Oxidation
Titanium
Bioactivity
Corrosion

ABSTRACT

In this study, the effects of GO-silane particles embedded into the oxide coating during Plasma Electrolytic Oxidation (PEO) of titanium on the growth mechanism, bioactivity, and corrosion properties were investigated. The results revealed that participation of GO-silane particles in titanium oxidation reactions led to the preparation of the oxide coating at higher responding voltages as well as the predominance of rutile over anatase. Introduction of the maximum amount of 5 $g.L^{-1}$ of GO-silane particles decreased the oxide coating thickness by about 51 % and increased its surface roughness up to around 48 %. The bioactivity of the oxide coating was improved by embedding GO-silane particles and consequently, the amount of induced calcium phosphate compounds increased. Compared to titanium in normal and inflammatory simulated body fluid, pure PEO-treated titanium promoted the polarization resistance and expanded the passivation region. Followed by incorporation of the GO-silane particles into the oxide coating, the protective function was weakened, hence the possibility of tailoring the corrosion properties according to the clinical applications.

https://doi.org/10.30501/acp.2022.364326.1106

1. INTRODUCTION

Titanium alloys are widely used to produce dental and orthopedic implants. Their biological superiority originates from the formation of a natural bioinert layer in the human body. Therefore, unlike bioactive materials such as bioglass and calcium phosphate ceramics, titanium alloys cannot form bone at the interface with the surrounding tissues [1,2]. To date, several techniques have been used for the surficial biological activation of titanium alloys, one of the newest of which is Plasma Electrolytic Oxidation (PEO) method. The PEO is a surface modification technique used for preparing oxide coatings which not only improves hardness, wear resistance, and chemical stability but provides a porous substrate for bone cell growth and proper implant adhesion. In this method, bioactive elements such as calcium, silicon, and strontium can be added to the structure of the oxide coating to promote its bioactivity [3-6].

Please cite this article as: Hamrahi, B., Yarmand, B., Massoudi, A., "Tailoring Bioactivity and Corrosion Properties of Plasma Electrolytic Oxidized Titanium Using GO-Silane Particles", ***Advanced Ceramics Progress***, Vol. 8, No. 4, (2022), 21-31. https://doi.org/10.30501/acp.2022.364326.1106

Silicon is the main element used for the proliferation and growth of connective tissues and bones and for this reason, the presence of silicon improves the bioactivity of implants as well as the proliferation of osteoblasts [7-9]. In the context of adding silicon to the PEO coatings, Zhao et al. [10] created the Si-doped TiO_2 coating. They reported that this coating promoted osteoblast adhesion, cell proliferation, and differentiation. In addition, they reported that the porous coating improved the initial stage of osseointegration and osteogenic ability of titanium implants in clinical performances. Yu et al. [11] studied the morphological changes of the PEO coatings prepared on Ti-6Al-4V in solutions containing calcium, phosphorus, strontium, and silicon ions. They found that addition of strontium and silicon increased the cell proliferation and bone-like apatite formation. In another study, Mumjitha et al. [12] prepared a TiO_2 coating that contained SiO_2 using sodium silicofluoride electrolyte. The immersion experiment in Simulated Body Fluid (SBF) clarified that compared to the pure TiO_2 coating, placement of SiO_2 could significanly promote bioactivity.

Carbon-based nanomaterials such as Graphene Oxide (GO) are a group of additives to PEO coatings capable of improving their properties greatly. Fattah-Alhosseini et al. reviewed the beneficial effects of graphene and GO additives on the corrosion properties and wear performance of the PEO coatings formed on titanium and magnesium [13,14]. Moreover, Chen et al. [15,16] reported that using graphene nanosheets in the silicate electrolyte promoted the corrosion behavior of magnesium and aluminum alloys. Zhao et al. [17] found that adding GO up to the optimum amount promoted the corrosion features of the PEO coating formed on magnesium. However, addition of excess amounts was found to weaken the corrosion resistance. Gao et al. [18] reported that upon adding GO to the PEO coating prepared on titanium, the corrosion features of the coating increased due to the blockage of the penetration path of corrosive ions. In another study, Bordbar-Khiabani et al. [19] found that followed by adding GO nanosheets to the coating prepared on titanium, the corrosion behavior would be significantly improved. Wen et al. [20] created an oxide coating containing HA/GO particles on magnesium using the PEO method. They reported enhancement in the corrosion properties of the oxide coating with particle placement and an increase in the polarization resistance. They also found that GO functional groups stimulated the biomineralization and bone regeneration.

This study aimed to investigate the effects of GO-silane particles on the growth of oxide coating on titanium using the PEO method for the first time. Moreover, the bioactivity and corrosion behavior of the prepared oxide coatings were evaluated in normal and inflammatory SBF.

2. MATERIALS AND METHODS

2.1. Synthesis of GO-Silane Particles

To synthesize GO-silane particles, GO nanosheets were produced through the modified Hummers method proposed in the previous work [19]. Silane particles were precipitated on the GO nanosheets through hydrolysis of tetraethyl orthosilicate. For this purpose, 30 mL of aqueous GO solution with the concentration of 0.4 $g.mL^{-1}$ was ultrasonically diluted with 300 mL of ethanol for 30 min. As a result, the pH of the solution increased up to 9 followed by adding ammonia. Next, 2 mL of tetraethyl orthosilicate was added to the previous solution and reacted ultrasonically for 1 h. The resulting precipitations were dried at 90 °C for 24 h.

2.2. Preparation of PEO Coatings

Commercially pure titanium was chosen as the substrate. The plate was cut in dimensions of 3 × 1 × 0.2 cm^3 and polished with silicon carbide papers. The coupons were rinsed with ethanol and exposed to hot air. The PEO was run using an alternating current power supply. Here, titanium was considered the anode, and the stainless-steel tube the cathode. Oxidation was achieved for 10 min at the constant current of 200 $mA.cm^{-2}$ in an electrolyte of 10 $g.L^{-1}$ Na_3PO_4 and 2 $g.L^{-1}$ KOH. The electrolyte was kept uniform during oxidation using stirring. To create coatings containing GO-silane particles, specific amounts of additives were first added to the based electrolyte and then mixed. The samples containing 0, 1, 3, and 5 $g.L^{-1}$ GO-silane particles were coded S0, S1, S3, and S5, respectively. The sample conditions are presented in Table 1.

TABLE 1. The specifications of the samples and electrolytes

Sample	Na_3PO_4 ($g.L^{-1}$)	KOH ($g.L^{-1}$)	GO-Silane ($g.L^{-1}$)	Conductivity ($mS.cm^{-1}$)	pH
S0	10	2	0	15.2	11.8
S1	10	2	1	14.6	12.1
S3	10	2	3	12.5	12.5
S5	10	2	5	11.4	12.6

2.3. Characterization Methods

The microstructure of the samples was studied using a Field Emission Scanning Electron Microscope (FESEM, TESCAN). The results from elemental analysis were then evaluated using Energy-Dispersive X-Ray Spectroscopy (EDS, OXFORD) at the accelerating voltage of 15 kV. The coating thickness was determined by measuring ten points via a Phynix thickness gauge. The coating roughness was measuring by determining six points at the center of the sample and three times in each of the horizontal and vertical axes using a Phynix contact roughness meter. Crystalline structure was characterized using Cu Kα X-ray. Chemical bonds were detected through Fourier Transform Infrared Spectroscopy (FTIR, Perkin Elmer).

2.4. In-vitro Bioactivity Expriment

The bioactivity test was done by immersing the specimens in the SBF. In this regard, the specimens were soaked vertically in a container containing 30 mL of SBF at 37 °C for 14 days based on Kokubo's method [21]. Thereafter, the specimens were rinsed, dried, and stored in a vacuum chamber.

2.5. Electrochemical Corrosion Test

Corrosion tests were conducted by a potentiostat galvanostat (EG & G) at 37 °C in both normal and inflammatory SBF. A standard cell with three electrodes was used for all corrosion tests. The Ag/AgCl electrode, the platinum plate, and samples were connected to the reference, auxiliary, and working electrodes, respectively. Then, 1 cm^2 of each specimen was exposed to the electrolyte. The potentiodynamic polarization experiment was performed in the limit potential of -1000 to 3000 mV compared to the open circuit potential with a sweep rate of 1 mV.s^{-1}, and the results were analyzed using CorrView software. The polarization resistance (R_p) was estimated based on Stern-Geary Equation (1), where β_c and β_a represent the cathodic and anodic slops, respectively. These parameters were calculated by extrapolating the potentiodynamic polarization graphs in the Tafel region. Inflammatory SBF was produced by adding 150 mM H_2O_2 and adjusting the pH at 5.2 using HCl solution.

$$R_p = \frac{\beta_a \times \beta_c}{2.3 \times i_{corr} \times (\beta_a + \beta_c)} \tag{1}$$

3. RESULTS AND DISCUSSION

3.1. Characterization of GO-Silane Particles

The microstructure of the synthesized GO and GO-silane particles is illustrated in Figures 1a and 1b. As observed in these figures, the GO particles have a layered microstructure. In the GO-silane, silane particles are almost densely and uniformly deposit on the carbon layers so that they cover the entire surface. Formation of the silane particles triggers use of hydrolysis and then condensation of the tetraethyl orthosilicate precursor and bonding with the oxygen groups of GO layers, thus leading to the nucleation and growth of particles. The EDS analysis presented in Figure 1c shows the presence of Si, O, and C, which confirms the synthesis and formation of the silane particles on the GO layers.

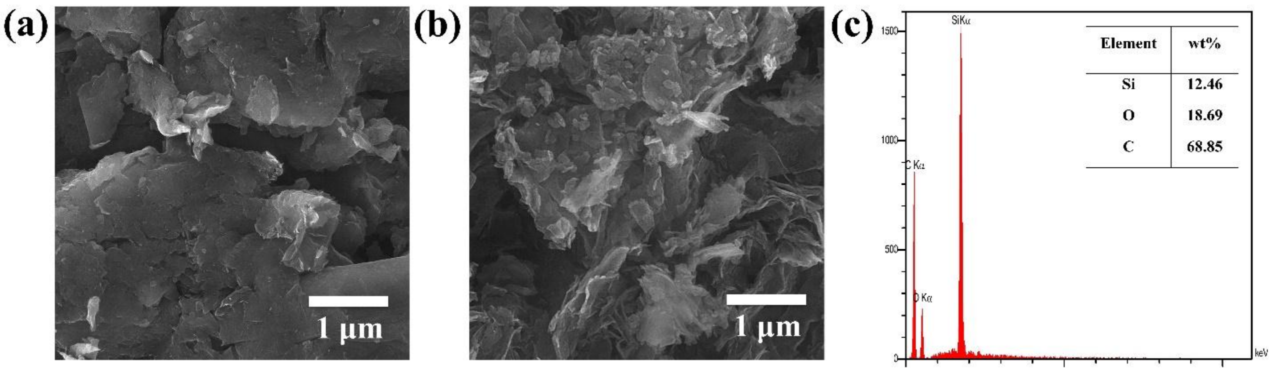

Figure 1. FESEM images of (a) GO and (b) GO-silane particles, and (c) EDS spectrum of GO-silane particles

The XRD patterns of the GO and GO-silane particles are illustrated in Figure 2a. In the XRD pattern of GO, only one sharp peak appears at 10.03° that corresponds to the (001) plane. This peak is very weak in the GO-silane pattern, which may be due to the destruction of the layered microstructure of GO during the synthesis of silane or the higher mass ratio of silane particles compared to GO. In the XRD pattern of GO-silane, a broad peak with low intensity appears at 24.3° that confirms the formation of silane with an amorphous structure [19,22]. The chemical bonds of GO and GO-silane particles detected by FTIR spectroscopy are displayed in Figure 2b where the C−O−C bands of the epoxy group appear at 1067 cm^{-1} and 1247 cm^{-1} in the GO spectrum. In addition, the C=C and C=O bands of carboxylic groups are observed at 1635 and 1744 cm^{-1}, respectively, which are all characteristics of GO.

In addition, the broad O−H band concentrates at 3424 cm^{-1}, which can be due to the adsorbed moisture.

In the spectrum of the GO-silane, new peaks appear at 470, 824, and 1100 cm^{-1}, which belong to the Si−O−Si band that result from the self-condensation of the silane bonds. Moreover, Si−OH and Si−O−C bands are located at 973 and 1249 cm^{-1}, respectively. The appearance of these bands simultaneous with the removal of epoxy and carboxyl bands is indicative of the reaction of silane bonds with the functional groups of GO. More detailed identification of GO and GO-silane chemical bonds is completed by Raman spectroscopy (Figure 2c). In both spectra, the D and G bands are located at 1355 and 1582 cm^{-1}, respectively. Furthermore, the 2D and D+G bands concentrate at 2700 and 2960 cm^{-1}, respectively. The fitted intensity ratio (I_D/I_G) with the Lorentzian function increases from 0.90 in GO to 0.96 in GO-silane, indicating the formation of covalent bonding of silane particles with GO layers along with the slight destruction of the carbon network [19,23,24].

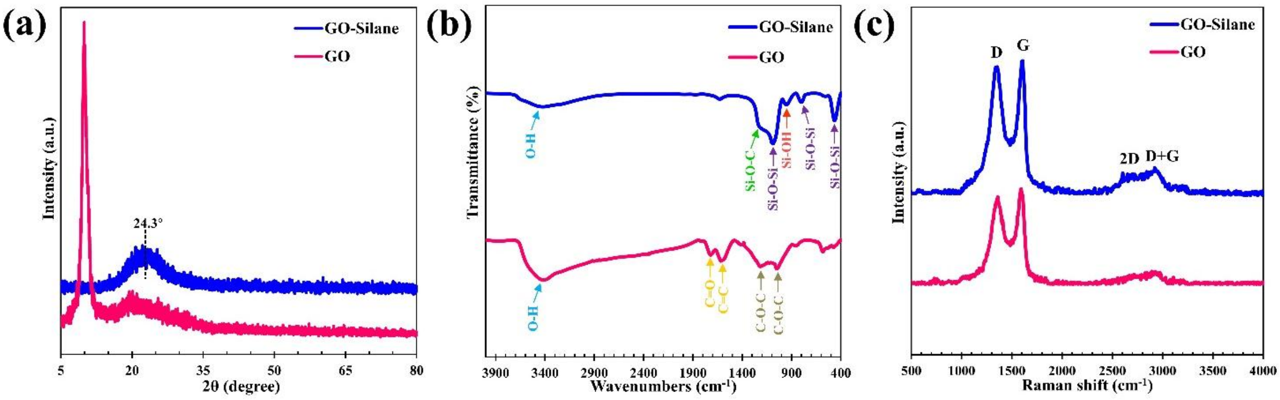

Figure 2. (a) XRD patterns, (b) FTIR, and (c) Raman spectra of GO and GO-silane particles

3.2. Responding Voltage During Oxidation

The responding voltage variations were studied to evaluate the effect of GO-silane particles on the formation mechanism of the oxide coating. Figure 3 shows the voltage changes as a function of process time for electrolytes containing different concentrations of GO-silane particles.

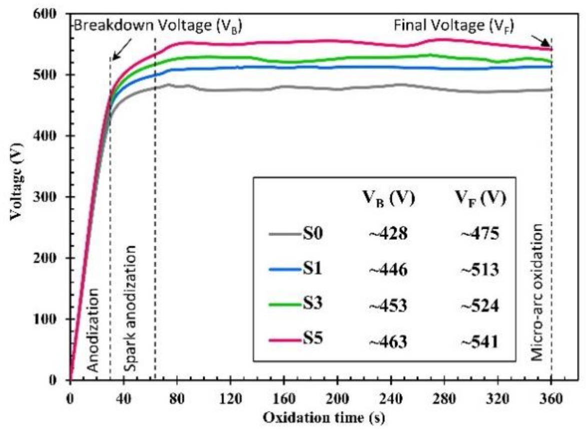

Figure 3. Voltage changes versus oxidation time

It is evident that the PEO process has three steps including the conventional anodization, spark anodization, and micro-arc oxidation [25]. In the first step, anodization occurs, which leads to a rapid linear increase in the voltage and involves the growth of a thin passive layer on titanium. The formation of the oxide layer occurs through the following reactions [26]:

$$Ti \leftrightarrow Ti^{2+} + 2e^- \quad (2)$$

$$H_2O \leftrightarrow O^{2-} + 2H^+ \quad (3)$$

$$2H_2O \leftrightarrow O_2 + 4H^+ + 4e^- \quad (4)$$

$$Ti^{2+} + 2O^{2-} \leftrightarrow TiO_2 + 2e^- \quad (5)$$

It is found that the growth of the primary oxide layer on the anode involves the penetration of O^{2-} from the oxide network to the oxide/metal interface as well as the reduction of oxygen at the electrolyte/oxide interface [25,27]. Given that all the curves have the same growth rate in this step, it can be concluded that addition of GO-silane particles does not have a considerable effect on the preparation of the oxide layer in the anodization step. Upon further increasing the responding voltage, gaseous products are formed, and the titanium surface is covered with a layer of insulating gas. The gas layer is ionized due to the electric field that eventually leads to the plasma formation at the electrolyte/oxide interface. At the same time, the porous oxide layer grows until the power of the electric field reaches a critical value and dielectric breakdown occurs. The second step (spark anodization) begins with the appearance of micro-sparks as well as increase in the voltage drop. Dielectric breakdown first begins in local defects in the oxide layer and finally spreads over the entire surface. According to the experimental model of Ikonopisov [28], the breakdown voltage (V_B) when the first sparks appear depends on the conductivity of the electrolyte (σ), as observed in Equation (6) where a_B and b_B are the constants associated with the material.

$$V_B = a_B + b_B \log (1/\sigma) \qquad (6)$$

The comparison of the curves in the second step reveals that the V_B enhances from 428 V in S0 to 446, 453, and 463 V in S1, S3, and S5, respectively. In addition, as shown in Table 1, with addition of the GO-silane particles, the electrolyte conductivity would decrease.

Followed by passing the V_B, the voltage rate slows down due to the occurrence of micro-sparks in a larger area of the oxide coating. In the third step (micro-arc oxidation), the responding voltage changes become more stable, and the oxide layer develops with repeated melting and freezing of the material. In fact, when the electric current passes through the discharge channel, some of the adjacent materials are melted and pushed out by the emitted gases. These substances will immediately freeze in contact with the electrolyte and accumulate in the opening of the channel and form the oxide layer. The micro-arc oxidation step has a similar process in all samples, and the responding voltage enhances with an increase in the number of GO-silane particles. The final voltage also changes according to the forming voltage [25,27].

3.3. Morphology and Chemical Analysis

The microstructure of the coatings is demonstrated in Figure 4. According to which, a rough oxide coating with many pores is created on the surface of all the specimens. The pores are originally formed due to the gas released by melting the compounds during the coating growth process. The frequent occurrence of micro-arcs and high energy discharges causes the local melting of the materials in the discharge channel, their eruption outside, and finally their rapid freezing by the cold electrolyte [27]. Introduction of GO-silane particles to the electrolyte changes the characteristics of pores as a result of which, more pores with smaller sizes are formed in S5 compared to S0. The formation of different microstructural features originates from the variations in the electrochemical reactions during the coating growth process, hence occurrence of further relative changes.

The coating composition was evaluated using EDS, the results of which are illustrated in Figure 4. The results confirm that Ti, O, and P are present in all coatings. Ti and O are the results of the participation of the substrate in the electrochemical interactions with the electrolyte, which leads to the titanium oxidation. According to the Albella model, the presence of P in all the coatings results from the entry of anionic electrolyte species in the electrochemical processes due to their electric charge [26]. Si and C are present in S1, and their values increase in S3 and S5. These results confirmed the formation of titanium oxide in all the coatings as well as the propoer placement of GO-silane particles. The elemental distribution of the coatings was checked using the EDS map of S5, the results of which are presented in Figure 5.

The analysis of the images revealed that all of the elements were uniformly distribute on the coating surface, and Si showed somewhat higher accumulation in the openings of the pores mainly due to the greater adsorption of GO-silane particles by electrostatic forces or their trapping in the eruptions of molten materials [4,27].

Figure 6 shows the FESEM cross-sectional microstructure of the specimens. As observed, all the coatings grew on the substrate surface without defects and gaps, hence well connected. The coating substrate interface in all samples is wavy that can be smoothed by increasing the concentration of GO-silane particles. This phenomenon occurs due to the non-uniform dissolution of titanium during electrochemical processes. A two-part microstructure, including the inner and outer sections, is

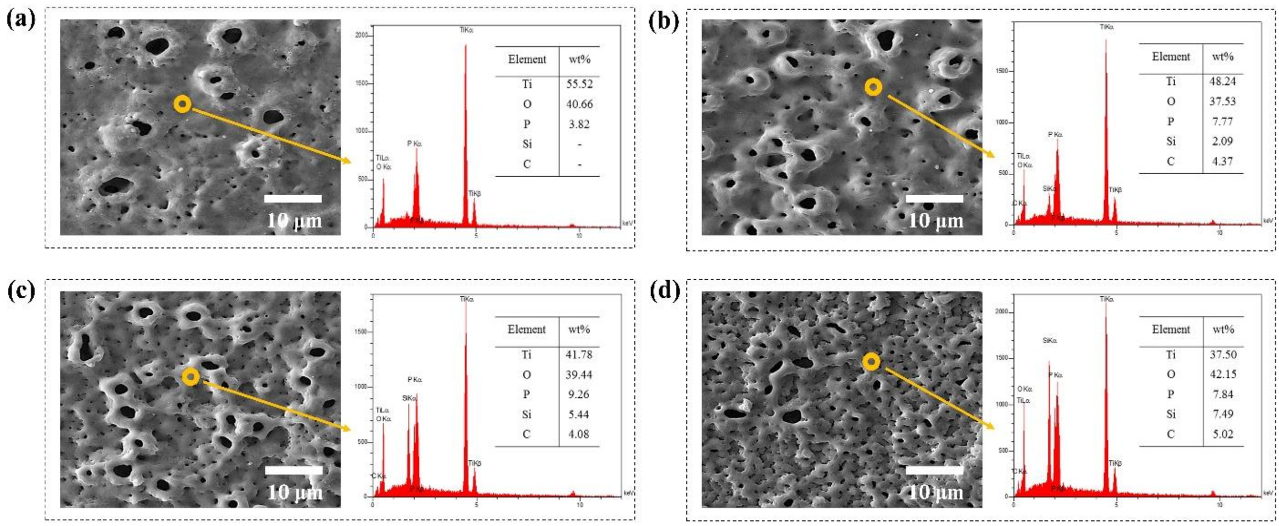

Figure 4. FESEM surface morphologies and corresponding EDS spectra of (a) S0, (b) S1, (c) S3, and (d) S5

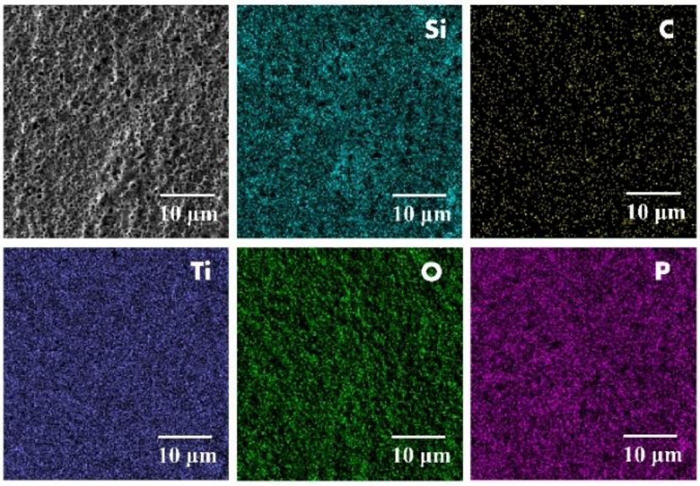

Figure 5. EDS elemental maps of S5

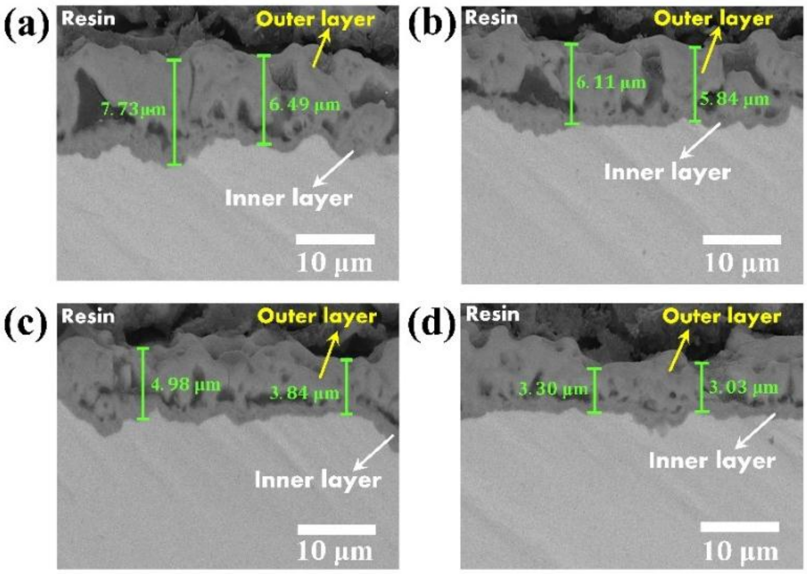

Figure 6. FESEM cross-sectional images of (a) S0, (b) S1, (c) S3, and (d) S5

observed in all of the coatings. The inner part that is less thick is in contact with titanium. The outer part is thicker than the inner part and therefore, it has more defects due to the occurrence of numerous micro-arcs. Upon increasing the concentration of GO-silane particles, the thickness of the coatings would decrease due to the change in the nature of the coating growth processes [27].

3.4. Thickness and Roughness

The thickness and roughness changes are displayed in Figure 7. According to the observations, upon increasing the concentration of the GO-silane particles, the thickness decreased from 7.18±0.87 µm in S0 to 3.55±0.38 µm in S5.

The surface roughness followed an upward trend, reching the value from 0.56±0.06 µm in S0 to 0.83±0.08 µm in S5. These results confirmd the FESEM observations.

In the PEO method, the oxide coating is repeatedly developed through the processes of local material melting, oxidation, and solidification due to micro-arcs occurring on the coating surface. In the case of the intensity enhancement of the micro-arcs, the resulting energy may destroy a large part of the previously formed oxide coating so that the amount of the new oxide layer cannot compensate for it. In this case, the growth rate of the layer was reduced, and smaller thickness values were obtained, similar to what happened in S1, S3, and S5. The increasing trend of roughness also confirmed the intensification of the oxide coating destruction processes, which is also in accordance with the responding voltage changes [25].

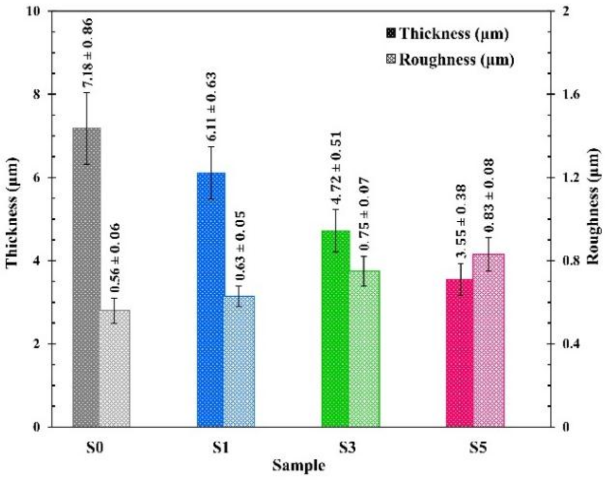

Figure 7. Thickness and surface roughness of the specimens

3.5. Crystal Structure

The XRD patterns of both S0 and S5 are demonstrated in Figure 8. The diffracted peaks were identified using the reference cards, clearly imploying that the peaks attributed to anatase, rutile, and titanium appeared in both samples. According to JCPDS card no. 001-0562, the peaks located at 29.6°, 56.8°, 63.7°, and 65.1° correspond to (101), (200), (105), and (105) planes of anatase, respectively. According to JCPDS card no. 004-0551, the peak that appeared at 32.1° belongs to the (110) plane of rutile. In addition, the peaks centered at 41.1°, 44.9°, 47.2°, 62.5°, 74.6°, and 84.4° are attributed to (100), (002), (101), (102), (110), and (103) planes of titanium, respectively, according to JCPDS card no. 044-1294. In both patterns, the peaks related to the compounds containing Si and Ti are not detected, indicating that the GO-silane particles are placed in the TiO_2 structure without reacting.

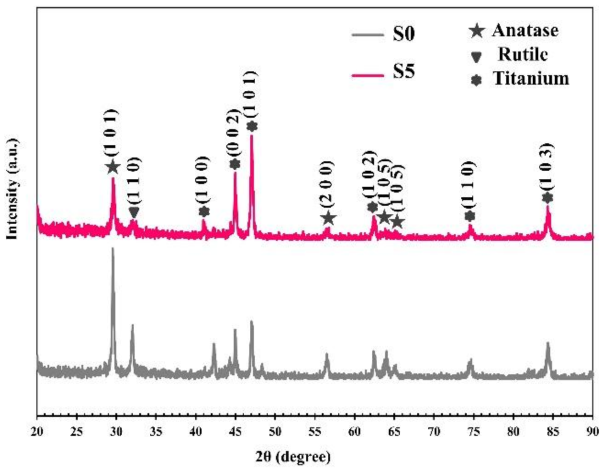

Figure 8. XRD patterns of S0 and S5

The intensity of the diffracted peaks in S5 decreased significantly, compared to those in S0, probably due to the crystal weakening of the oxide phases and reduction of the coating thickness. The volume ratio of anatase (X_A) and rutile (X_R) is estimated through the following relationships [29]:

$$X_A = \frac{1}{1 + 1.265(I_R/I_A)} \tag{7}$$

$$X_R = 1 - X_A \tag{8}$$

where I_R and I_A are the intensities of the characteristic (110) and (101) planes of rutile and anatase, respectively.

It was found that the ratio of anatase to rutile decreased from 0.79 in S0 to 0.51 in S5. The phase transformation of anatase to rutile can be affected by the change in the characteristics of micro-arcs and heat produced during the growth of the oxide coating. The local temperature increase inside the discharge channels may provide the thermodynamic conditions required for the phase transformation [25,27].

3.6. In-Vitro Bioactivity

The surface morphology of the coatings after 14 days of immersion in normal SBF is displayed in Figure 9. As observed, nanometer precipitations were formed in a tiny amount on S0. The number of precipitations rised with the enhancement in the concentration of GO-silane particles; therefore the largest number of precipitations is deposited in S5 in the form of relatively spherical agglomerated particles.

The EDS results presented in Figure 9 confirm that calcium phosphate compounds are formed on all of the coatings. The amount of calcium and phosphorus as well as their ratio (Ca/P) increased with an increase in the GO-silane concentration, hence improvement of the bioactivity of the coatings along with the better stability of calcium phosphate precipitations. An increase in the amount of calcium phosphate compounds resulted from embedding Si in the oxide coating, the triggering factor for precipitation. Indeed, Ti−OH and Si−OH functional groups with a negative charge are created on the surface of the coatings due to their placement in the SBF. These groups positively adsorb the charged calcium ions in the SBF and facilitate the formation of calcium compounds. Next, these calcium compounds bind with the negative phosphate ions and form calcium phosphate. When the nuclei of hydroxyapatite are created, they became a uniform and dense layer by adsorbing calcium and phosphorus ions of the SBF. Moreover, the rougher surface of the oxide coating can play an influential role in providing nucleation sites for precipitations. Therefore, it can be concluded that addition of the GO-silane particles to the PEO-treated titanium coating improves its bioactive feature, which will also lead to faster proliferation and growth of the bone cells [30-33].

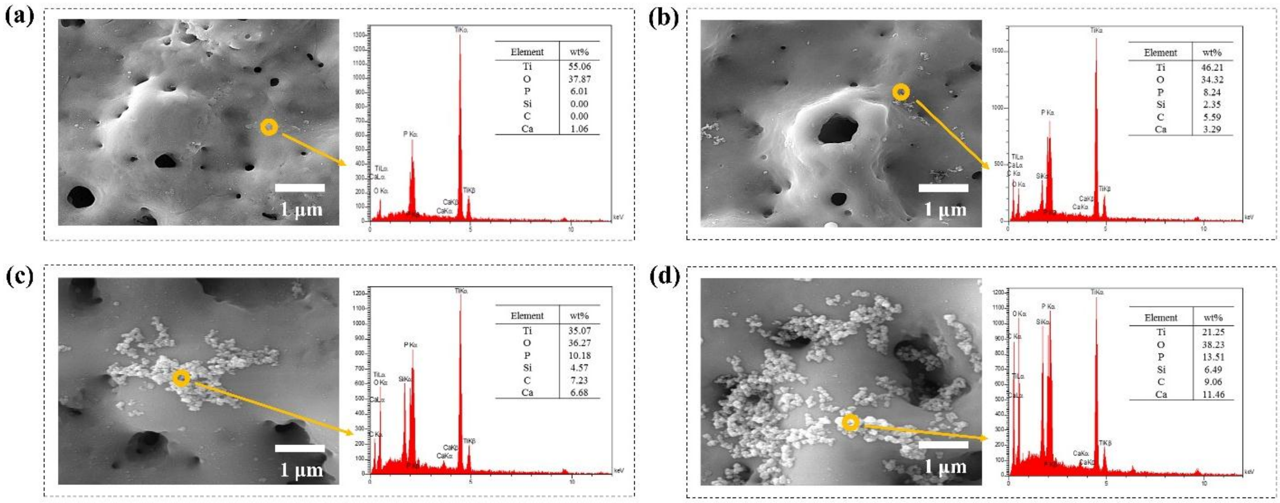

Figure 9. FESEM images and EDS spectra of (a) S0, (b) S1, (c) S3, and (d) S5 after immersion in normal SBF

3.7. Corrosion Properties

The corrosion properties of the specimens were investigated through the potentiodynamic polarization experiments at 37 °C in normal and inflammatory SBF. Figure 10 illustrates the potentiodynamic polarization graphs of the coatings as well as titanium. Corrosion characteristics estimated from the curves are presented in Table 2. A passive region is observed in all of the curves in the normal and inflammatory SBF.

The passive region for titanium in normal SBF ranges approximately from 239 to 1800 mV, which becomes wider with the preparation of PEO coating, S0 from -54 to 2102 mV, S1 from -105 to 2021 mV, S3 from -195 to 1950 mV, and S5 from -201 to 1770 mV. Since no coating failure is observed in any of the specimens, it can be found that the coatings exhibit proper pitting corrosion resistance in normal SBF. The passive current density in S0 decreases by one order of magnitude compared to titanium; however, it increased slightly compared to S0 (Table 2) followed by adding the GO-silane particles. The lower values of the passive current density of the coatings are indicative of the improvement in their corrosion resistance, compared to titanium [34,35].

In addition, the comparison of the data in Table 2 showed that S0 was characterized by better corrosion features than those of titanium and consequently, the R_p increased from 23.47 up to 61.92 kΩ.cm^2 due to the protective power of the PEO coating, which prevents dissolution by blocking the path of corrosive ions toward the substrate.

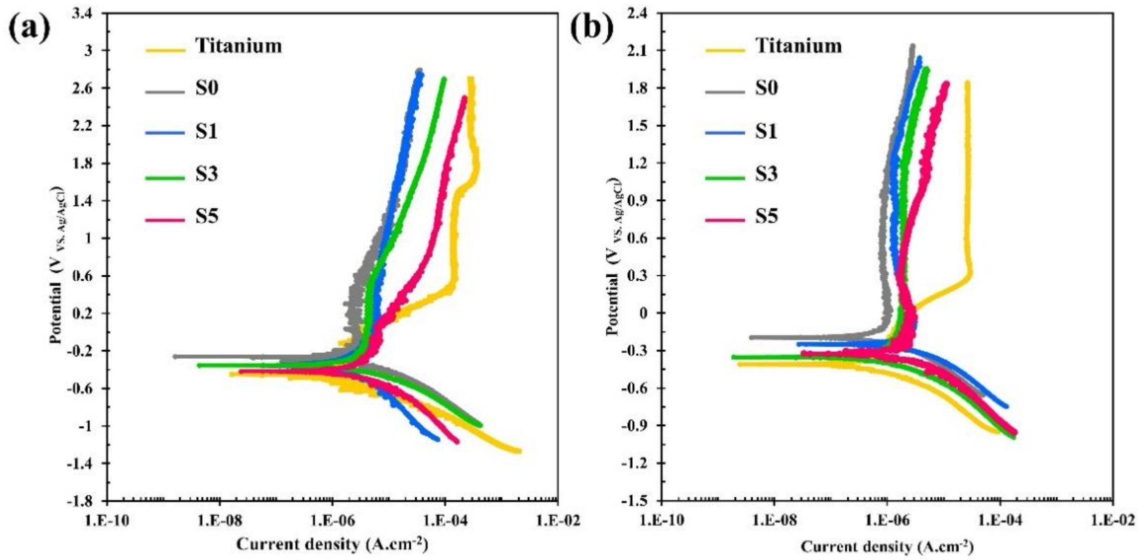

Figure 10. Potentiodynamic polarization graphs of the specimens in (a) normal and (b) inflammatory SBF

TABLE 2. Corrosion characteristics derived from potentiodynamic polarization graphs

Medium	Sample	E_{corr} (mV)	i_{corr} (A.cm^{-2})	β_c (mV.dec^{-1})	β_a (mV.dec^{-1})	Rp (Ω.cm^2)	$I_{passive}$ (A.cm^{-2})
Normal SBF	Ti	-408.85	2.21E-6	295.15	203.01	23470	2.57E-5
	S0	-194.84	1.24E-6	289.22	455.21	61920	7.28E-7
	S1	-249.28	3.27E-6	310.31	432.85	23990	1.33E-6
	S3	-353.26	4.11E-6	341.41	426.55	20030	1.84E-6
	S5	-350.11	4.74E-6	315.74	421.41	16530	1.34E-6
Inflammatory SBF	Ti	-474.28	4.89E-6	272.38	232.28	11130	1.32E-4
	S0	-258.58	3.56E-6	197.35	625.34	18290	2.40E-6
	S1	-360.11	5.21E-6	264.54	511.14	14520	4.12E-6
	S3	-351.26	6.10E-6	186.41	513.11	9730	3.97E-6
	S5	-416.21	6.85E-6	241.98	364.59	9210	4.71E-6

Followed by placing the GO-silane particles in the PEO coating, the corrosion characteristics will be degraded, indicating the deterioration of the stability of the coatings. This phenomenon can be directly caused by the reduction of the coating thickness, leading to less obstruction of the path of aggressive species. Moreover, an increase in the roughness is another influential factor because it increases the physical adsorption of corrosive ions [34,36,37].

In the polarization curve of titanium in inflammatory SBF, a narrower passive region appears from 442 to 1413 mV compared to normal SBF. In this region, an oxidation reaction starts at 1641 mV, and re-passivation occurs at 1955 mV. Such observations were already reported in the studies of Sowa et al. and Metikoš-Huković et al. during titanium polarization in Ringer's and Hanks' solutions, respectively [35,38]. In addition, the effect of inflammatory conditions on titanium includes shifting the corrosion potential to more negative values (from -408.85 to -474.28 mV) and increasing the corrosion current density (from 2.21E-6 to 4.89E-6 A.cm^{-2}) along with the instability of the passive region.

Once the PEO coating is prepared, the R_p of titanium improved from 11130 to 18290 Ω.cm^2 in the inflammatory SBF, which is lower than the normal SBF.

The harsher conditions of the inflammatory medium made the passive region of the coatings become more unstable so that the coatings became passive at first and then, the passive layer failed. According to the reports of Yerokhin et al., this phenomenon resulted from the formation of metastable compounds due to the rapid melting and solidification of oxides during the PEO process.

These substances were subjected to oxidation or even degradation in the corrosive solution during the potentiodynamic polarization scan as a result of which, the thinning of the coating, which was intensified in the inflammatory SBF, occured [27,39]. Reduction of the corrosion rate by placing GO-silane particles in the coatings was also observed in the inflammatory SBF.

4. CONCLUSIONS

1. The intervention of the GO-silane particles in the processes of coating formation led to the intensification of micro-arcs as well as an increase in the responding voltage.
2. As a result of the rise in the energy from micro-arcs, the anatase-rutile transformation progressed.
3. Upon adding GO-silane particles, the coating thickness followed a decreasing trend while the coating surface roughness followed an increasing trend.
4. Placement of GO-silane particles induced the calcium phosphate precipitations on the oxide coating and improved its bioactivity.
5. Creation of the oxide coating on titanium led to different values of corrosion resistance in the normal and inflammatory SBF, thus making it possible to achieve features suitable for biological usages.

ACKNOWLEDGEMENTS

This research has been supported via grant No.: 247383 by Materials and Energy Research Center, Karaj, Iran.

REFERENCES

1. Matykina, E., Arrabal, R., Mingo, B., Mohedano, M., Pardo, A., Merino, M. C., "In vitro corrosion performance of PEO coated Ti and Ti6Al4V used for dental and orthopaedic implants", ***Surface and Coatings Technology***, Vol. 307, (2016), 1255-1264. https://doi.org/10.1016/j.surfcoat.2016.08.018
2. Berbel, L. O., Banczek, E. D. P., Karoussis, I. K., Kotsakis, G. A., Costa, I., "Determinants of corrosion resistance of Ti-6Al-4V alloy dental implants in an In Vitro model of peri-implant

inflammation", ***PLOS ONE***, Vol. 14, No. 1, (2019), e0210530. https://doi.org/10.1371/journal.pone.0210530

3. Hussein, R. O., Nie, X., Northwood, D. O., "The application of plasma electrolytic oxidation (PEO) to the production of corrosion resistant coatings on magnesium alloys: a review", ***Corrosion and Materials***, Vol. 38, No. 1, (2013), 55-65. https://doi.org/10.1007/s11661-018-4824-8
4. Fattah-Alhosseini, A., Keshavarz, M. K., Molaei, M., Gashti, S. O., "Plasma electrolytic oxidation (PEO) process on commercially pure Ti surface: effects of electrolyte on the microstructure and corrosion behavior of coatings", ***Metallurgical and Materials Transactions A***, Vol. 49, No. 10, (2018), 4966-4979. https://doi.org/10.1007/s11661-018-4824-8
5. Fattah-alhosseini, A., Molaei, M., Babaei, K., "The effects of nano-and micro-particles on properties of plasma electrolytic oxidation (PEO) coatings applied on titanium substrates: A review", ***Surfaces and Interfaces***, Vol. 21, (2020), 100659. https://doi.org/10.1016/j.surfin.2020.100659
6. Aliofkhazraei, M., Macdonald, D. D., Matykina, E., Parfenov, E. V., Egorkin, V. S., Curran, J. A., Troughton, S. C., Sinebryukhov, S. L., Gnedenkov, S. V., Lampke, T., Simchen, F., "Review of plasma electrolytic oxidation of titanium substrates: Mechanism, properties, applications and limitations", ***Applied Surface Science Advances***, Vol. 5, (2021), 100121. https://doi.org/10.1016/j.apsadv.2021.100121
7. Pietak, A. M., Reid, J. W., Stott, M. J., Sayer, M., "Silicon substitution in the calcium phosphate bioceramics", ***Biomaterials***, Vol. 28, No. 28, (2007), 4023-4032. https://doi.org/10.1016/j.biomaterials.2007.05.003
8. Wang, B., Sun, J., Qian, S., Liu, X., Zhang, S., Liu, F., Dong, S., Zha, G., "Proliferation and differentiation of osteoblastic cells on silicon-doped TiO_2 film deposited by cathodic arc", ***Biomedicine & Pharmacotherapy***, Vol. 66, No. 8, (2012), 633-641. https://doi.org/10.1016/j.biopha.2012.08.008
9. Toorani, M., Aliofkhazraei, M., Mahdavian, M., Naderi, R., "Effective PEO/Silane pretreatment of epoxy coating applied on AZ31B Mg alloy for corrosion protection", ***Corrosion Science***, Vol. 169, (2020), 108608. https://doi.org/10.1016/j.corsci.2020.108608
10. Zhao, Q. M., Li, X. K., Guo, S., Wang, N., Liu, W.W., Shi, L., Guo, Z., "Osteogenic activity of a titanium surface modified with silicon-doped titanium dioxide", ***Materials Science and Engineering***, Vol. 110, (2020), 110682. https://doi.org/10.1016/j.msec.2020.110682
11. Yu, J. M., Choe, H. C., "Morphology changes and bone formation on PEO-treated Ti-6Al-4V alloy in electrolyte containing Ca, P, Sr, and Si ions", ***Applied Surface Science***, Vol. 477, (2019), 121-130. https://doi.org/10.1016/j.apsusc.2017.11.223
12. Mumjitha, M., Raj, V., "Fabrication of TiO_2–SiO_2 bioceramic coatings on Ti alloy and its synergetic effect on biocompatibility and corrosion resistance", ***Journal of the Mechanical Behavior of Biomedical Materials***, Vol. 46, (2015), 205-221. https://doi.org/10.1016/j.jmbbm.2015.02.006
13. Fattah-alhosseini, A., Chaharmahali, R., "Enhancing corrosion and wear performance of PEO coatings on Mg alloys using graphene and graphene oxide additions: A review", ***FlatChem***, Vol. 27, (2021), 100241. https://doi.org/10.1016/j.flatc.2021.100241
14. Fattah-alhosseini, A., Molaei, M., Nouri, M., Babaei, K., "Review of the role of graphene and its derivatives in enhancing the performance of plasma electrolytic oxidation coatings on titanium and its alloys", ***Applied Surface Science Advances***, Vol. 6, (2021), 100140. https://doi.org/10.1016/j.apsadv.2021.100140
15. Chen, F., Zhang, Y., Zhang, Y., "Effect of graphene on micro-structure and properties of MAO coating prepared on Mg-Li alloy", ***International Journal of Electrochemical Science***, Vol. 12, No. 7, (2017), 6081-6091. https://doi.org/10.20964/2017.07.59
16. Chen, Q., Jiang, Z., Tang, S., Dong, W., Tong, Q., Li, W., "Influence of graphene particles on the micro-arc oxidation behaviors of 6063 aluminum alloy and the coating properties", ***Applied Surface Science***, Vol. 423, (2017), 939-950. https://doi.org/10.1016/j.apsusc.2017.06.202
17. Zhao, J., Xie, X., Zhang, C., "Effect of the graphene oxide additive on the corrosion resistance of the plasma electrolytic oxidation coating of the AZ31 magnesium alloy", ***Corrosion Science***, Vol. 114, (2017), 146-155. https://doi.org/10.1016/j.corsci.2016.11.007
18. Gao, Y., Yang, W., Xu, D., Chen, J., Jiang, B., "Microstructure and properties of graphene oxide-doped TiO_2 coating on titanium by micro arc oxidation", ***Journal of Wuhan University of Technology-Mater. Sci. Ed.***, Vol. 33, No. 6, (2018), 1524-1529. https://doi.org/10.1007/s11595-018-2001-y
19. Bordbar-Khiabani, A., Ebrahimi, S., Yarmand, B., "Highly corrosion protection properties of plasma electrolytic oxidized titanium using rGO nanosheets", ***Applied Surface Science***, Vol. 486, (2019), 153-165. https://doi.org/10.1016/j.apsusc.2019.05.026
20. Wen, C., Zhan, X., Huang, X., Xu, F., Luo, L., Xia, C., "Characterization and corrosion properties of hydroxyapatite/graphene oxide bio-composite coating on magnesium alloy by one-step micro-arc oxidation method", ***Surface and Coatings Technology***, Vol. 317, (2017), 125-133. https://doi.org/10.1016/j.surfcoat.2017.03.034
21. Kokubo, T., Takadama, H., "How useful is SBF in predicting in vivo bone bioactivity?", ***Biomaterials***, Vol. 27, No. 15, (2006), 2907-2915. https://doi.org/10.1016/j.biomaterials.2006.01.017
22. Kou, L., Gao, C., "Making silica nanoparticle-covered graphene oxide nanohybrids as general building blocks for large-area superhydrophilic coatings", ***Nanoscale***, Vol. 3, No. 2, (2011), 519-528. https://doi.org/10.1039/C0NR00609B
23. Wu, H., Tang, B., Wu, P., "Development of novel SiO_2–GO nanohybrid/polysulfone membrane with enhanced performance", ***Journal of Membrane Science***, Vol. 451, (2014), 94-102. https://doi.org/10.1016/j.memsci.2013.09.018
24. Zhang, W. L., Choi, H. J., "Silica-graphene oxide hybrid composite particles and their electroresponsive characteristics", ***Langmuir***, Vol. 28, No. 17, (2012), 7055-7062. https://doi.org/10.1021/la3009283
25. Yerokhin, A. L., Nie, X., Leyland, A., Matthews, A., Dowey, S. J., "Plasma electrolysis for surface engineering", ***Surface and Coatings Technology***, Vol. 122, No. 2-3, (1999), 73-93. https://doi.org/10.1016/S0257-8972(99)00441-7
26. Venkateswarlu, K., Rameshbabu, N., Sreekanth, D., Sandhyarani, M., Bose, A. C., Muthupandi, V., Subramanian, S., "Role of electrolyte chemistry on electronic and in vitro electrochemical properties of micro-arc oxidized titania films on Cp Ti", ***Electrochimica Acta***, Vol. 105, (2013), 468-480. https://doi.org/10.1016/j.electacta.2013.05.032
27. Yerokhin, A. L., Nie, X., Leyland, A., Matthews, A., "Characterisation of oxide films produced by plasma electrolytic oxidation of a Ti–6Al–4V alloy", ***Surface and Coatings Technology***, Vol. 130, No. 2-3, (2000), 195-206. https://doi.org/10.1016/S0257-8972(00)00719-2
28. Ikonopisov, S., "Theory of electrical breakdown during formation of barrier anodic films", ***Electrochimica Acta***, Vol. 22, No. 10, (1977), 1077-1082. https://doi.org/10.1016/0013-4686(77)80042-X
29. Venkateswarlu, K., Rameshbabu, N., Sreekanth, D., Bose, A. C., Muthupandi, V., Babu, N. K., Subramanian, S., "Role of electrolyte additives on in-vitro electrochemical behavior of micro arc oxidized titania films on Cp Ti", ***Applied Surface Science***, Vol. 258, No. 18, (2012), 6853-6863. https://doi.org/10.1016/j.apsusc.2012.03.118
30. Shin, K. R., Ko, Y. G., Shin, D. H., "Influence of zirconia on biomimetic apatite formation in pure titanium coated via plasma electrolytic oxidation", ***Materials Letters***, Vol. 64, No. 24, (2010), 2714-2717. https://doi.org/10.1016/j.matlet.2010.08.069
31. Ahmadi, A., Ramezanzadeh, B., Mahdavian, M., "Hybrid silane coating reinforced with silanized graphene oxide nanosheets with improved corrosion protective performance", ***RSC Advances***,

Vol. 6, No. 59, (2016), 54102-54112. https://doi.org/10.1039/C6RA04843A

32. Molaei, M., Fattah-alhosseini, A., Nouri, M., Mahmoodi, P., Nourian, A., "Incorporating TiO_2 nanoparticles to enhance corrosion resistance, cytocompatibility, and antibacterial properties of PEO ceramic coatings on titanium", ***Ceramics International***, Vol. 48, No. 14, (2022), 21005-21024. https://doi.org/10.1016/j.ceramint.2022.04.096
33. Nikoomanzari, E., Fattah-alhosseini, A., Karbasi, M., Nourian, A., "A versatile TiO_2/ZrO_2 nanocomposite coating produced on Ti-6Al-4V via plasma electrolytic oxidation process", ***Surfaces and Interfaces***, Vol. 32, (2022), 102128. https://doi.org/10.1016/j.surfin.2022.102128
34. Marques, I. D. S. V., Barão, V. A. R., da Cruz, N. C., Yuan, J. C. C., Mesquita, M. F., Ricomini-Filho, A. P., Sukotjo, C., Mathew, M. T., "Electrochemical behavior of bioactive coatings on cp-Ti surface for dental application", ***Corrosion Science***, Vol. 100, (2015), 133-146. https://doi.org/10.1016/j.corsci.2015.07.019
35. Sowa, M., Simka, W., "Electrochemical behavior of plasma electrolytically oxidized niobium in simulated physiological environment", ***Surface and Coatings Technology***, Vol. 344, (2018), 121-131. https://doi.org/10.1016/j.surfcoat.2018.03.013
36. Hwang, I. J., Choe, H. C., "Effects of Zn and Si ions on the corrosion behaviors of PEO-treated Ti-6Al-4V alloy", ***Applied Surface Science***, Vol. 477, (2019), 79-90. https://doi.org/10.1016/j.apsusc.2017.12.015
37. Nikoomanzari, E., Fattah-alhosseini, A., Alamoti, M. R. P., Keshavarz, M. K., "Effect of ZrO_2 nanoparticles addition to PEO coatings on Ti–6Al–4V substrate: Microstructural analysis, corrosion behavior and antibacterial effect of coatings in Hank's physiological solution", ***Ceramics International***, Vol. 46, No. 9, (2020), 13114-13124. https://doi.org/10.1016/j.ceramint.2020.02.084
38. Metikos-Huković, M., Kwokal, A., Piljac, J., "The influence of niobium and vanadium on passivity of titanium-based implants in physiological solution", ***Biomaterials***, Vol. 24, No. 21, (2003), 3765-3775. https://doi.org/10.1016/S0142-9612(03)00252-7
39. Molaei, M., Fattah-alhosseini, A., Nouri, M., Mahmoodi, P., Navard, S. H., Nourian, A., "Enhancing cytocompatibility, antibacterial activity and corrosion resistance of PEO coatings on titanium using incorporated ZrO_2 nanoparticles", ***Surfaces and Interfaces***, Vol. 30, (2022), 101967. https://doi.org/10.1016/j.surfin.2022.101967